NANO LETTERS

Letter

pubs.acs.org/NanoLett

Quantifying and Elucidating Thermally Enhanced Minority Carrier Diffusion Length Using Radius-Controlled Rutile Nanowires

Liming Zhang,[†] Litianqi Sun,[†] Zixuan Guan,[‡] Sangchul Lee,[†] Yingzhou Li,[§] Haitao D. Deng,[†] Yiyang Li,[†] Nadia L. Ahlborg,[†] Madhur Boloor,[†] Nicholas A. Melosh,[†] and William C. Chueh*[,†]

[†]Department of Materials Science & Engineering, [‡]Department of Applied Physics, [§]Institute for Computational & Mathematical Engineering (ICME), Stanford University, Stanford, California 94305, United States

Supporting Information

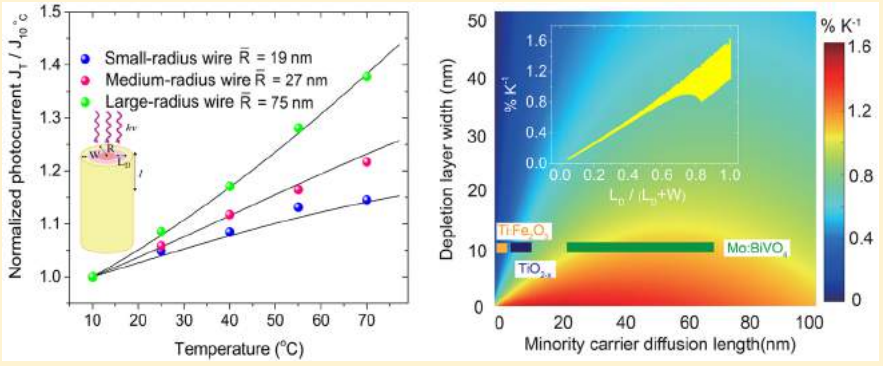

ABSTRACT: The minority carrier diffusion length (L_D) is a crucial property that determines the performance of light absorbers in photoelectrochemical (PEC) cells. Many transition-metal oxides are stable photoanodes for solar water splitting but exhibit a small to moderate L_D, ranging from a few nanometers (such as α-Fe_2O_3 and TiO_2) to a few tens of nanometers (such as $BiVO_4$). Under operating conditions, the temperature of PEC cells can deviate substantially from ambient, yet the temperature dependence of L_D has not been quantified. In this work, we show that measuring the photocurrent as a function of both temperature and absorber dimensions provides a quantitative method for evaluating the temperature-dependent minority carrier transport. By measuring photocurrents of nonstoichiometric rutile TiO_{2-x} nanowires as a function of wire radius (19−75 nm) and temperature (10−70 °C), we extract the minority carrier diffusion length along with its activation energy. The minority carrier diffusion length in TiO_{2-x} increases from 5 nm at 25 °C to 10 nm at 70 °C, implying that enhanced carrier mobility outweighs the increase in the recombination rate with temperature. Additionally, by comparing the temperature-dependent photocurrent in $BiVO_4$, TiO_2, and α-Fe_2O_3, we conclude that the ratio of the minority carrier diffusion length to the depletion layer width determines the extent of temperature enhancement, and reconcile the widespread temperature coefficients, which ranged from 0.6 to 1.7% K^{-1}. This insight provides a general design rule to select light absorbers for large thermally activated photocurrents and to predict PEC cell characteristics at a range of temperatures encountered during realistic device operation.

KEYWORDS: *Photoelectrochemistry, temperature-dependent, minority carrier diffusion length, TiO_2 nanowires, thermally activated photocurrent*

Transition-metal-oxide (TMO) semiconductors are promising photoelectrodes for solar water splitting due to their excellent chemical stability.[1,2] However, the charge carrier mobilities in these light absorbers are often very low (typically $\leq$1 $cm^2\ V^{-1}\ s^{-1}$), because the carriers are either trapped (due to electron-defect coupling) or localized as small polarons (due to electron−lattice coupling).[3−6] Additionally, the high doping level required to achieve sufficient majority carrier conductivity in TMOs leads to a small depletion region width (W, typically several to a few tens of nanometers).[7] Therefore, a significant fraction of the light is absorbed in the quasi-neutral region, and the photocurrent yield is primarily determined by the minority carrier diffusion length (L_D).[7] Recently, it was shown that the oxygen-evolution reaction (OER) photocurrent of $BiVO_4$ and α-Fe_2O_3 increased with temperature, which was hypothesized to arise from the thermally activated minority carrier mobility.[8,9] Interestingly, the extent of temperature enhancement varied significantly between TMOs (1.7% K^{-1} for $BiVO_4$ and 0.6% K^{-1} for α-Fe_2O_3, both for sulfite oxidation), the origin of which is not yet fully understood.

Temperature variations in PEC cells occur naturally through infrared heating, which is moreover exploited directly in aqueous[8,9] and solid-state electrolyte cells[10,11] at temperatures below and above ~100 °C, respectively. However, despite its

Received: April 10, 2017
Revised: July 15, 2017
Published: August 17, 2017

DOI: 10.1021/acs.nanolett.7b01504
Nano Lett. 2017, 17, 5264−5272

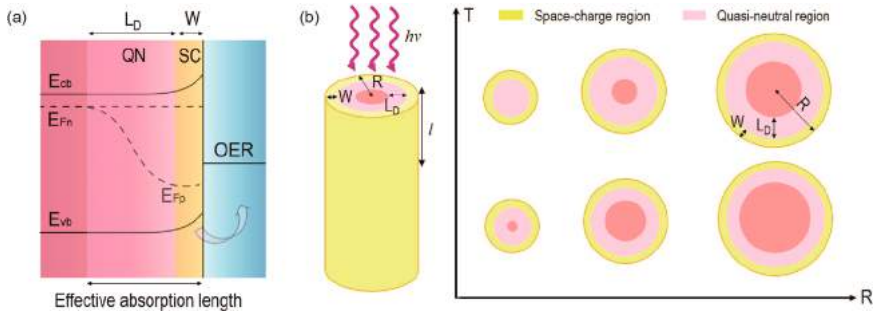

Figure 1. Dependence of the photocurrent on both temperature and radius of an ideal, cylindrical nanowire. (a) A schematic illustration of the Schottky junction on the semiconductor−electrolyte interface, showing the space-charge region (SC) and the quasi-neutral region (QN). (b) A schematic illustration of the relationship between the space-charge layer thickness (W), minority carrier diffusion length (L_D), and nanowire radius (R) as a function of temperature. In nanowires with a small radius (left column), the effective absorption length at elevated temperatures approaches R, leading to a plateau of the photocurrent with temperature. In the medium- and large-radius nanowires, the effective absorption length is smaller than R for all of the temperatures examined, leading to an increase of the photocurrent with temperature.

importance, the temperature dependence of L_D has not been quantified, and therefore its impact on photocurrent is not well-understood. For example, in device models, the temperature dependence of L_D is usually not considered.[12] Accounting for the temperature dependence of L_D is necessary to correctly predict and optimize the behavior of PEC devices based on both aqueous and solid-state electrolytes, especially those involving electrocatalytic processes with large activation barriers, such as CO_2 reduction. Electron-beam induced current[13−15] and spectral response[16−18] techniques have been employed to determine L_D in semiconductors at room temperature. Recently, Pala et al. also reported a technique that employs a wedge-shaped, rear-illuminated sample geometry.[19]

In this work, we develop and validate a general method for evaluating the temperature-dependent minority carrier diffusion length in light absorbers. An analytical, one-dimensional model describes the dependence of the photocurrent on both temperature and radius of nanowires. We apply this model to nonstoichiometric, rutile TiO_{2-x} nanowires, a widely studied photoanode for OER that exhibits a large bandgap (∼3.0 eV),[20] a moderate carrier lifetime (∼40 ns),[21] and a short L_D at room temperature (RT, ∼10 nm).[22] The majority carrier mobility of rutile TiO_2 is ∼1 $cm^2\ V^{-1}\ s^{-1}$ at RT and exhibits an activation energy of ∼0.2 eV.[20] The minority carrier mobility at RT can be estimated from L_D and carrier lifetime, which yields a mobility on the order of 10^{-3} $cm^2\ V^{-1}\ s^{-1}$, consistent with a hopping conduction mechanism. The minority carrier diffusion length L_D, along with its activation energy E_a, was quantitatively extracted from temperature-dependent photocurrents measured for various wire radii. We confirm that L_D increases with temperature, which implies that the increase in the minority carrier mobility with temperature outweighs the decrease in the carrier lifetime. From our model, we also developed simple selection rules for semiconductors that exhibit significant thermally enhanced photocurrent, and link the different temperature-dependent behaviors in three low-mobility oxide photoanodes ($BiVO_4$, TiO_2, and α-Fe_2O_3) to the relative magnitudes of L_D and W.

In low-mobility oxides, photons not absorbed in the space-charge region enter the adjacent quasi-neutral region where the minority carrier mobility and lifetime determine the charge carrier collection efficiency (Figure 1a). In a nanowire geometry, we expect that both L_D and the wire radius (R) determine the photoactivity. As illustrated schematically in Figure 1b, for a given wire R, increasing L_D (through temperature, T, for example) increases the fraction of the wire that is photoactive. When L_D extends to the entire radius of the wire, a further increase in L_D will not have an effect on the photocurrent. This suggests that measuring photocurrent as a function of both temperature and wire radius can yield the temperature-dependent L_D.

Therefore, we develop an analytical model that describes the dependence of the photocurrent (j) on both temperature and radius of an ideal, cylindrical nanowire. For simplicity, we assume that L_D depends on temperature in an Arrhenius manner ($L_D(T) = L_0 \exp\left(-\frac{E_a}{kT}\right)$, where L_0 is the prefactor and k is the Boltzmann constant) and that W depends on temperature negligibly. We also assume that the majority carrier transport is fast (typically satisfied for photoelectrodes with a high-doping level). We further neglect recombination at the electrode/electrolyte interface (a good approximation when employing a hole scavenger[23−25]). Finally, we assume that material properties, both of the bulk and of the surface, do not change with wire radius.

We build on the wire model derived in literature[26] and introduce a temperature-dependent L_D. The complete derivation is documented in the Supporting Information. Briefly, the photocurrent flowing through the wire consists of two components: one due to the generation of carriers within the depletion layer W, and one due to the generation of carriers in the bulk that diffuse into the depletion layer. Assuming that all the carriers generated in the depletion region contribute to the current, it is given by

$$j_{dep} = q\varphi_0\pi(1 - e^{-\alpha L})[R^2 - (R - W)^2] \quad (1)$$

where L is the wire length, q is the charge transferred per carrier, φ_0 is the total photon flux, and α is the absorption coefficient. The diffusion contribution, on the other hand, is obtained by solving the diffusion equation for holes with suitable boundary conditions. The diffusion current is given by

$$j_{diff} = q\varphi_0\pi(1 - e^{-\alpha L})\left[2(R - W)L_D(T)\frac{I_0'\left(\frac{R-W}{L_D(T)}\right)}{I_0\left(\frac{R-W}{L_D(T)}\right)}\right] \quad (2)$$

DOI: 10.1021/acs.nanolett.7b01504
Nano Lett. 2017, 17, 5264−5272

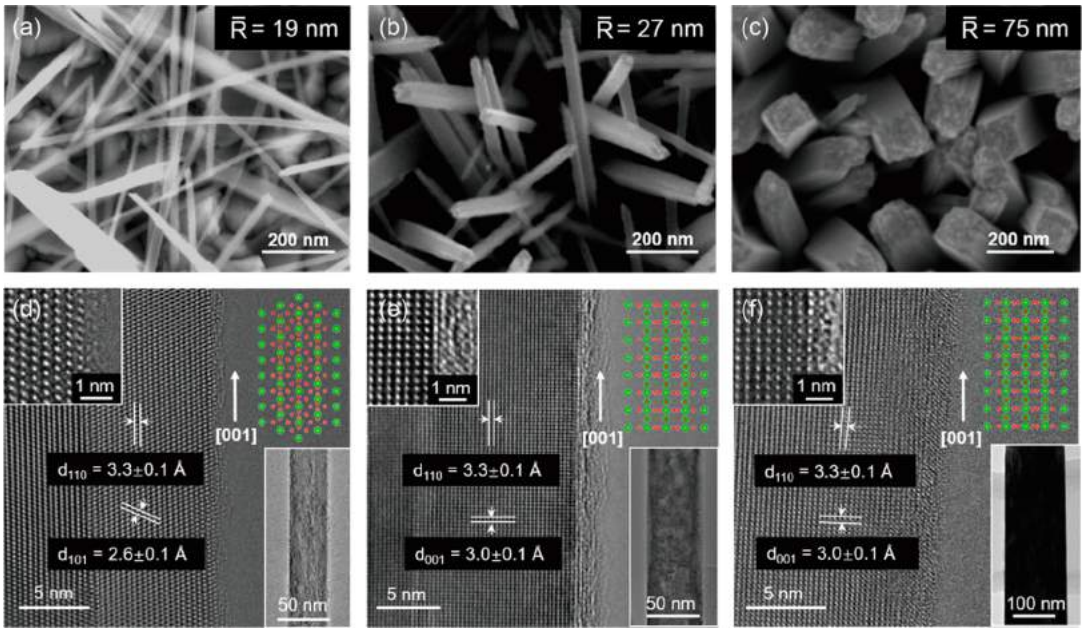

Figure 2. Radius-controlled TiO_{2-x} nanowires. (a–c) Top-view SEM images of TiO_{2-x} nanowire array on FTO with small (a), medium (b), and large (c) radius. (d–f) High-resolution TEM (HRTEM) images of a single TiO_2 nanowire with small (d), medium (e), and large (f) radius. Insets: high-magnification images of the nanowire surface, low-resolution TEM images, and structural models. Green and red spheres represent Ti and O atoms, respectively. The growth direction of the wires is along [001] direction, and the zone axis is [1, −1, −1] for the small wire (d) and [1, −1, 0] for the medium and large wires (e–f). The contrast in the TEM images across the bulk of nanowire could be due to defect formation during the synthesis.

where I_0 is the modified Bessel's function of the first kind, and $I_0' = \frac{1}{L_D}\frac{\partial I_0}{\partial r}$, where r is the distance to the wire surface in the radial direction (see Supporting Information for details). Combining the two contributions, we obtain the photocurrent in a single nanowire at a given temperature T for $R > W$. When $R \leq W$, the nanowire is fully photoactive radially, and the total photocurrent j is given by

$$j = q\varphi_0\pi(1 - e^{-\alpha L})R^2 \quad (3)$$

To eliminate proportionality constants and to remove the uncertainties due to sample-to-sample variations, we normalize the photocurrent at a given temperature by the photocurrent at T_{ref}:

$$\frac{J(T)}{J(T_{ref})} = \frac{\sum j(T)}{\sum j(T_{ref})} = \frac{\int_0^{+\infty} j(T)f(R)\,dR}{\int_0^{+\infty} j(T_{ref})f(R)\,dR} \quad (4)$$

where $f(R)$ characterizes the distribution of the wire radius (taken to be Gaussian, see Supporting Information) to account for the polydispersity. We note that the absorption coefficient can depend weakly on temperature. However, in the limit of $L \gg \alpha^{-1}$, the nanowire absorbs all of the incident photons, which makes the temperature effect on α negligible. We will discuss two temperature coefficients (unit of % K^{-1}): the instantaneous temperature coefficient, defined as the local slope of $J(T)/J(T_{ref})-T$ curve, and the average temperature coefficient, defined as the average photocurrent enhancement across the temperature range examined. Next, we experimentally measure the photocurrent temperature coefficient as a function of T and R, and fit the model to obtain L_0 and E_a.

We fabricated oriented and uniform rutile TiO_2 nanowires with different radii and comparable lengths on F-doped SnO_2/glass substrate (FTO) via a hydrothermal route.[27,28] The fast growth rate along the [001] direction leads to stable c-elongated anisotropic nanowires dominated by {110} surfaces.[27] As such, the wire radius can be controlled by chemically tuning the growth rate on {110} surfaces. Under standard growth conditions using a 0.6 mM titanium isopropoxide (TTIP) precursor (see Methods for details), we obtained nanowires with a Gaussian radius distribution (Supporting Information, Figure S1). The average radius ($\bar{R}$) is 27 nm, and the standard deviation (σ) is 11 nm (Figure 2b). Adding saturated aqueous NaCl solution during synthesis leads to a preferential Cl^- adsorption on {110} surfaces and suppresses the radial growth.[27] Using this approach, we obtained nanowires with $\bar{R}$ = 19 nm (σ = 7 nm) (Figure 2a). On the other hand, increasing the concentration of TTIP in the solution from 0.6 to 0.9 mM increases the radius to 75 nm (σ = 25 nm) (Figure 2c). The nanowire lengths, tuned by adjusting the growth time, are approximately 1.6 μm for all three growth conditions. This wire length is substantially longer than α^{-1}, and thus light absorption is not limiting and does not affect the temperature dependence of the photocurrent.

To eliminate the overpotential due to majority carrier transport, we reduced the nanowires at 375 °C in flowing H_2:H_2O = 800:1 (see Methods for details).[29,30] On the basis of literature thermogravimetric data,[31,32] this condition gives an oxygen vacancy concentration of approximately 0.03 mol % (assuming negligible oxidation during cooling) and an increase in the majority carrier concentration by 2×10^{19} cm^{-3} (see details in Supporting Information and Figure S4). We confirmed that the majority carrier transport is not limiting by measuring the OER photocurrent as a function of wire length and reduction conditions under front and back illumination (Supporting Information, Figures S2–3).

High-resolution transmission electron microscopy (HRTEM) confirms that the reduced nanowires exhibit a

DOI: 10.1021/acs.nanolett.7b01504
Nano Lett. 2017, 17, 5264–5272

single-crystalline rutile structure with preferential growth along the [001] direction (Figures 2d–e). There is no change in the lattice parameters with radius/synthesis condition, which is additionally confirmed by the X-ray diffraction (XRD) (Table 1 and Supporting Information, Figure S5). No impurity phase was detected by XRD (Supporting Information, Figure S6). Importantly, we also do not observe a significantly different surface structure for the three types of nanowire (insets of Figures 2d–e). This observation suggests that the primary difference between the nanowires is the radius, a key assumption in our model. The detailed information for all three wires is listed in Table 1.

Table 1. Radius, Length, and Lattice Constants of TiO_{2-x} Nanowires

	wire radius		wire length		lattice constants (tetragonal)	
	average value (nm)	standard deviation (nm)	average value (μm)	standard deviation (μm)	a (Å)	c (Å)
small radius	19	7	1.6	0.2	4.594	2.958
medium radius	27	11	1.6	0.1	4.594	2.958
large radius	75	25	1.6	0.1	4.594	2.958
ref. (JCPDS No. 21-1276)					4.593	2.959

Having optimized the TiO_{2-x} nanowire lengths and majority carrier concentration, we first examined the temperature dependence of the photoelectrochemical properties of the nanowires with $\bar{R}$ = 27 nm. At 25 °C, we observe an onset potential (defined as the potential that gives a current density of 0.01 mA cm^{-2}) of 0.24 V vs RHE and a photocurrent of 1.2 mA cm^{-2} at 1.23 V vs RHE (Figures 3a and c). The photoactivity of TiO_{2-x} increases monotonically with temperature, with the saturation photocurrent (at 1.23 V vs RHE) increasing from 1.1 mA cm^{-2} at 10 °C to 1.4 mA cm^{-2} at 70 °C. The average temperature coefficient is 0.5% K^{-1}. The photocurrent is reversible on cooling (Figure 3b), confirming the temperature enhancement effect. The photocurrent is stable for 10 h at 70 °C (Supporting Information, Figure S7).

To assess the relative contribution of thermally activated electrocatalysis (typically assumed to be the cause for current thermal-enhancement in device models[12]) versus thermally activated minority carrier transport, we also characterized the TiO_{2-x} photoactivity for sulfite oxidation, in which the surface recombination arising from the slow transfer kinetics of holes at the interface is negligible (Supporting Information, Figure S8).[23−25] We observe that the saturation photocurrent is identical with and without the sulfite hole scavenger. This indicates that all of the holes reaching the TiO_{2-x} surface participate in the OER, even without catalysts.[33] Therefore, we attribute the thermally activated photocurrent to the improved minority carrier collection rather than improved electrocatalysis.

Turning to the onset potential, it shifts anodically at a rate of 1.7 mV K^{-1}, which is significantly smaller than the decrease of photovoltage with temperature, 4.0 mV K^{-1} (Figure 3c). The photovoltage is defined as the change of the open circuit potential under dark vs illumination and is measured using a

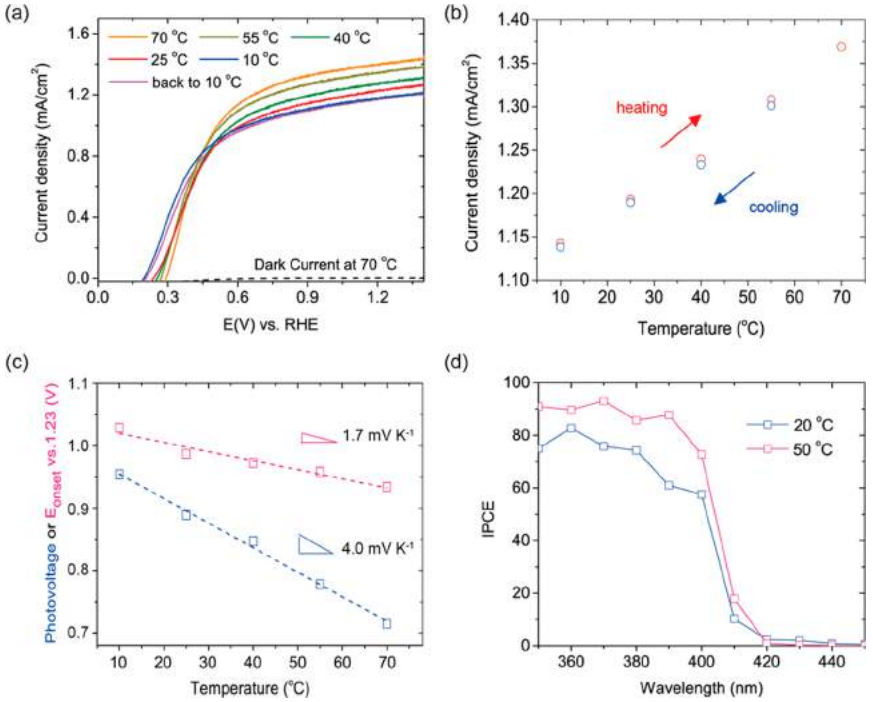

Figure 3. Thermally enhanced photocurrent in TiO_{2-x} nanowires with $\bar{R}$ = 27 nm. (a) Temperature-dependent photocurrent–voltage curves of TiO_{2-x} photoanode under 1 sun illumination in a 1 M NaOH electrolyte. Dark current does not depend significantly on temperature in the range of 0.0–1.23 V vs RHE. (b) The photocurrent measured in the current–voltage curves under different temperatures at 1.23 V vs RHE during heating and cooling. (c) Temperature dependence of the photovoltage (blue) and onset potential (red). Lines represent linear fits. The onset potential was defined at a current density of 0.01 mA cm^{-2}. (d) Temperature-dependent IPCE measurement carried out at 1.0 V vs RHE under 1 sun background light in a 1 M NaOH electrolyte with 0.1 M Na_2SO_3.

DOI: 10.1021/acs.nanolett.7b01504
Nano Lett. 2017, 17, 5264–5272

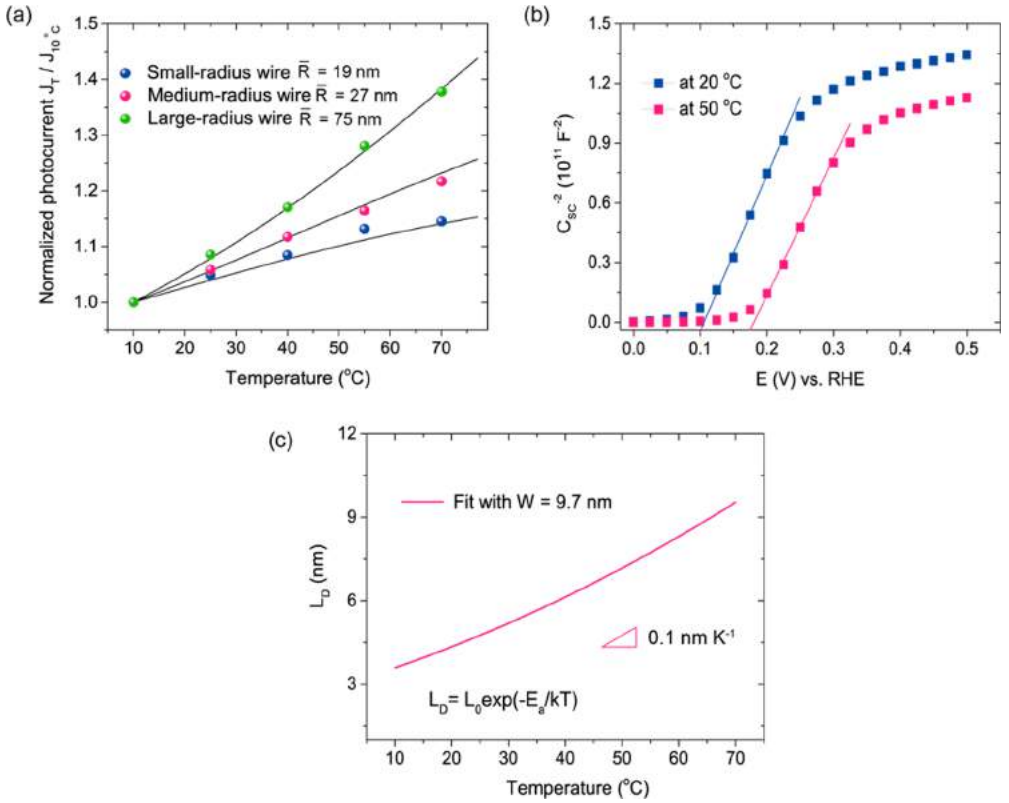

Figure 4. Radius- and temperature-dependent photocurrent. (a) Comparison of the photocurrent normalized to that at 10 °C (at 1.0 V vs RHE) as a function of temperature for TiO_{2-x} nanowires with different radii under 1 sun illumination in a 1 M NaOH electrolyte with 0.1 M Na_2SO_3. For all three TiO_{2-x} wire radii, the saturation photocurrent increases monotonically with temperature (see Supporting Information, Figure S11). The solid lines represent the nonlinear fitting of the photocurrent temperature coefficients. (b) Mott–Schottky plots measured in a 1 M NaOH electrolyte at the frequency of 1 kHz on a TiO_{2-x} photoanode under different temperatures. Solid lines represent fits of the corresponding linear regions. (c) Temperature-dependent minority carrier diffusion length L_D, calculated based on $L_D(T) = L_0 \exp\left(-\frac{E_a}{kT}\right)$, where L_0 and E_a are obtained from fitting the data in (a) with W = 9.7 nm.

ferri/ferrocyanide reversible redox couple (1 mM $[Fe(CN)_6]^{3-}$/ 10 mM $[Fe(CN)_6]^{4-}$ in a 1 M NaOH electrolyte), which approximates the equilibrium redox potential to OER.[34] (see Methods and Supporting Information, Figure S9). The difference arises because thermodynamics and kinetics of the OER, in addition to the photovoltage, contribute to the temperature dependence of the onset potential.[35−40] For completeness, we also measured the temperature dependence of the incident photon-to-current efficiency (IPCE) at 1.0 V vs RHE in sulfite solution by varying the wavelength of a small-magnitude monochromatic light superimposed on a 1 sun solar spectrum (Figure 3d). IPCE at 390 nm approached 88% at 50 °C, increased from 61% at 20 °C. Integrating the IPCE curves over all wavelengths gives values that agree with the photocurrent under broadband illumination (Supporting Information, Figure S10).

On the basis of our analytical model, the temperature-dependent minority carrier diffusion length can be extracted by varying both temperature and wire radius. We measured the photocurrent–voltage curves of nanowires with $\bar{R}$ of 19, 27, and 75 nm at temperatures between 10 and 70 °C. All measurements were carried out in the presence of the sulfite hole scavenger to eliminate the overpotential from electrocatalysis, though it was shown to be negligible at RT as discussed previously. For all three TiO_{2-x} wires, the saturation photocurrent increases monotonically with temperature (Supporting Information, Figure S11). However, the instantaneous temperature coefficient (i.e., slope of the line in Figure 4a) varies significantly with the wire radius and also with temperature. Whereas the saturation current density for the $\bar{R}$ = 75 nm nanowires increases linearly with temperature (with an average coefficient of 0.7% K^{-1}), it is sublinear for the smaller-radius nanowires. Specifically, for the $\bar{R}$ = 27 and 19 nm nanowires, the photocurrent plateaus with temperature, resulting in lower average temperature coefficients: 0.4% K^{-1} and 0.3% K^{-1}, respectively. In particular, for the smallest nanowires examined, the photocurrent essentially stopped increasing with temperature above 55 °C.

We also estimated the temperature-dependent space-charge layer width using the Mott–Schottky analysis in the dark (1 kHz, Figure 4b; other frequencies, Supporting Information, Figure S12). The band potential V_{fb}, obtained by fitting the curves in the linear region, shifts from 0.11 to 0.18 V vs RHE when the temperature increases from 20 to 50 °C. The majority carrier concentration (N_D), also obtained from fitting the curves in the linear region, increases from 0.97×10^{20} to 1.1×10^{20} cm^{-3}. The width of the space-charge layer is given by $W = \sqrt{\frac{2\varepsilon_0\varepsilon_r(V - V_{fb} - KT/e)}{eN_D}}$, where ε_r and ε_0 are the relative permittivity of TiO_{2-x} and the permittivity in vacuum, respectively, V is the applied potential, and e is the elementary charge. At 1.0 V vs RHE, we estimate that W decreases from 10.1 to 9.3 nm when the temperature increases from 20 to 50 °C, essentially temperature-independent.

DOI: 10.1021/acs.nanolett.7b01504
Nano Lett. 2017, 17, 5264−5272

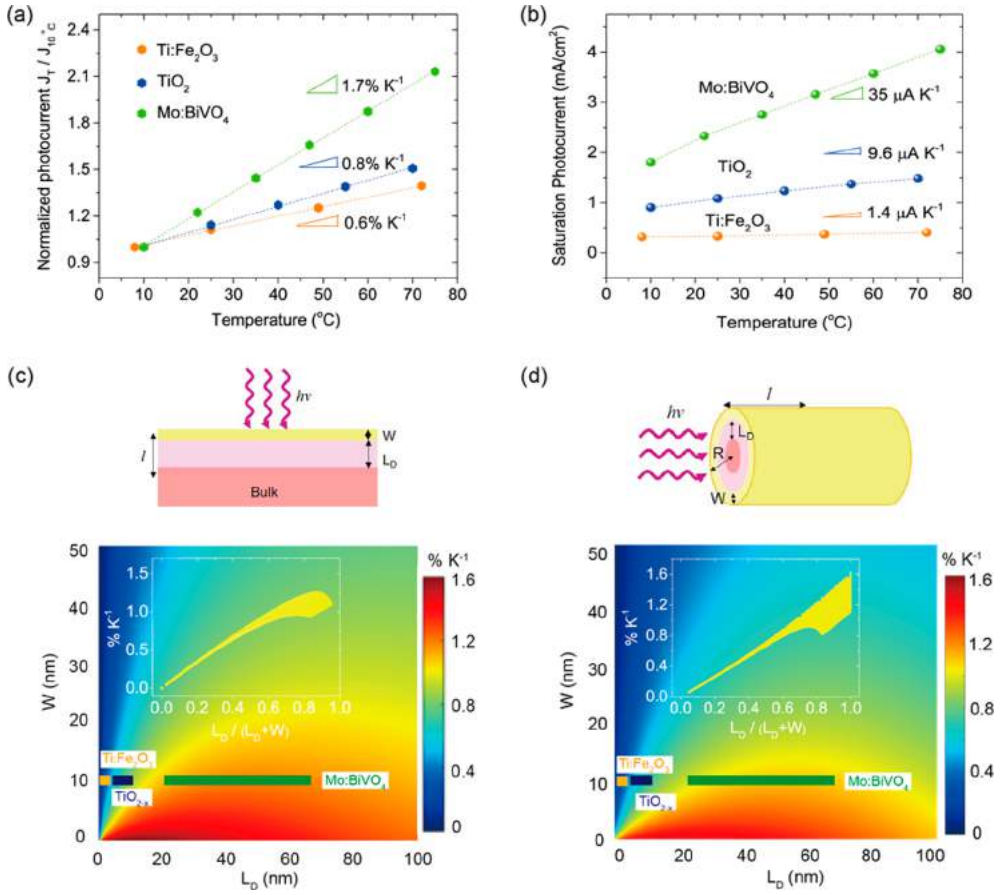

Figure 5. Parametric analysis of the thermally enhanced photocurrent using both planar and wire geometries. (a) Comparison of the photocurrent temperature coefficients (normalized to the current density at 10 °C) for three oxide light absorbers. The photocurrent was measured at 1.0 V vs RHE on 1% Mo-doped $BiVO_4$ in a 0.5 M phosphate buffer solution, 1.23 V vs RHE on 0.1% Ti-doped α-Fe_2O_3 and TiO_{2-x} in 1 M NaOH. In both electrolytes, 0.1 M Na_2SO_3 was added as a hole scavenger. The dashed lines are linear fits. The average photocurrent coefficients are also shown. (b) Comparison of the saturation photocurrent as a function of temperature under 1 sun illumination. The measurement conditions are identical to (a). (c) The instantaneous photocurrent temperature coefficient $[dj^{(\lambda)}/dT]/j_{10°C}$ in planar geometry (shown in the schematic illustration), at 298 K, as a function of the minority carrier diffusion length L_D and the width of space charge layer W, assuming $\alpha = 5 \times 10^5$ cm^{-1} and an activation energy E_a = 0.1 eV. The inset plots in (c) shows the photocurrent enhancement as a function of $L_D/(L_D + W)$. (d) The instantaneous photocurrent temperature coefficient $[dj^{(\lambda)}/dT]/j_{10°C}$ in the wire geometry (shown in the schematic illustration), at 298 K, as a function of L_D and W, when R is 300 nm (see Supporting Information, Figure S14 for additional simulations for different R). We assume the activation energy E_a = 0.1 eV. The inset plots in (d) shows the photocurrent enhancement as a function of $L_D/(L_D + W)$. The photocurrent is more sensitive to the temperature when L_D is much larger than W. The inset solid boxes in (c) and (d) demonstrate the positions for α-Ti:Fe_2O_3, TiO_{2-x}, and Mo:$BiVO_4$ on the color map, respectively.

Having measured the temperature dependence of the photocurrent as well as the space-charge layer width, we first discuss the data qualitatively and then fit the analytical model. For the $\bar{R}$ = 75 nm nanowires, the linear $J-T$ curve indicates that the radius is larger than the effective length for minority carrier collection at all temperatures examined. For the smaller-radius nanowires, at a threshold temperature, the effective length for minority carrier collection reaches a value that is comparable to the wire radius, giving rise to curvature in the photocurrent temperature coefficient (Figure 1b). In other words, the entire wire is photoactive radially. We note that a complete saturation with temperature is not observed because of the distribution of wire radii.

We fit the model (eq 4) to the temperature- and radius-dependent photocurrent in Figure 4a to extract L_D, using the experimentally measured radius distribution. As the Mott–Schottky analysis reveals that the space-charge layer width depends negligibly on temperature, we approximate it as a constant for the temperature range examined, 9.7 nm. A single set of fitting parameters (L_0 and E_a) was used to describe all points in Figure 4a simultaneously. The nonlinear least-squares, shown in Figure 4a, is excellent. Fitting errors were examined rigorously using a Jacobian approach (see Supporting Information for details). We obtain an activation energy E_a of 0.14 ± 0.01 eV and a prefactor L_0 of 958 ± 93 nm (i.e., L_D at T → ∞). Using these parameters, we calculated L_D as a function of temperature (Figure 4c). At 25 °C, L_D = 5.0 ± 0.9 nm, which doubles to 9.5 ± 1.8 nm at 70 °C. Indeed, the change in the minority carrier diffusion length with temperature is much greater than that of the space-charge width measured in the dark. Importantly, the positive activation energy of the minority carrier diffusion length confirms that thermal activation of the hole mobility outweighs the decrease of carrier lifetime with temperature. For completeness, we also perform the fit with W (taken as temperature-independent) as an additional fitting parameter. We obtain an activation energy E_a of 0.09 ± 0.01 eV, a prefactor L_0 of 237 ± 101 nm, and a space-charge layer width W of 7.6 ± 1.5 nm. We note that setting W = 0 also gives a reasonable fit (Supporting Information, Figure S13).

DOI: 10.1021/acs.nanolett.7b01504
Nano Lett. 2017, 17, 5264–5272

Now that we have validated the model describing the thermally enhanced photocurrent in radius-controlled rutile nanowires, we use it to reconcile the different behaviors of three commonly investigated, low-mobility oxide photoanodes (Mo:$BiVO_4$, TiO_{2-x} and α-Ti:Fe_2O_3). Like TiO_2, $BiVO_4$, and Fe_2O_3 are both polaronic oxides that exhibit an Arrhenius-manner minority carrier transport.[3,5] Our model does not consider the majority carrier transport limitation. For Mo:$BiVO_4$, comparison of the photocurrent under front and back illumination confirmed that this is the case.[8] For Ti:Fe_2O_3, a thin and dense film structure with a thickness of ~30 nm (deposited by pulsed-laser deposition) renders majority carrier transport facile.[9,41] In both cases, the dopant levels were chosen to give sufficient majority carrier concentrations. The model also neglects carrier recombination at the electrode/electrolyte interface, an assumption that is satisfied experimentally for the three photoelectrodes by employing a hole scavenger solution. As shown in Figure 5a, the average photocurrent coefficient varies dramatically between these three materials: 1.7% K^{-1} in Mo:$BiVO_4$, 0.8% K^{-1} in TiO_{2-x}, and 0.6% K^{-1} in α-Ti:Fe_2O_3. The thermally activated current in TiO_{2-x} is about half that of Mo:$BiVO_4$, which is recognized as a photoelectrode with significant thermal activation. Although the temperature coefficient of TiO_{2-x} nanowire may not be as significant as other photoelectrodes, measuring its temperature-dependent properties validated our new measurement method of L_D and explained how its temperature dependence is connected to that of the photocurrent. The absolute photocurrent enhancement in these three photoanodes differs even more: 35, 9.6, and 1.4 μA K^{-1}, respectively (Figure 5b), owing to the different RT saturation photocurrent between three photoanodes.

A parametric analysis of the model is shown in Figure 5c and d, using thin film (Figure 5c) and nanowire (Figure 5d) geometries, respectively (see Supporting Information for details). These two figures plot the instantaneous photocurrent temperature coefficient as a function of L_D and W, assuming that majority carrier transport, recombination, electrocatalysis, and light absorption are not limiting (satisfied for the measurements considered here). A temperature coefficient plot vs $L_D/(L_D + W)$ is also shown as an inset in Figures 5c–d. These plots show that the ratio of L_D to W establishes the extent of temperature enhancement in light absorbers exhibiting Arrhenius-type minority carrier diffusion length. When $L_D/(L_D + W)$ is small, the photocurrent is insensitive to temperature, because most of the minority carriers are collected from the temperature-independent depletion region. However, when $L_D/(L_D + W)$ is large, the photocurrent is very sensitive to temperature because a majority of charge carriers are collected from the temperature-enhanced quasi-neutral region.

Finally, we use the parametric analysis to understand the broad extent of temperature enhancements observed in Mo:$BiVO_4$, TiO_{2-x}, and α-Ti:Fe_2O_3. Due to the high doping level in all three materials, W is similar, on the order of 10–20 nm. However, L_D differs significantly. For instance, the L_D of Mo or W doped $BiVO_4$ at RT is reported to be in the range of 20–100 nm (depending on the sample preparation methods, doping concentrations and measurement techniques),[5,42−44] which is much larger than that of reduced rutile TiO_2 (5–10 nm),[22] and α-Ti:Fe_2O_3 (2–4 nm)[45] (see Supporting Information, Table S3 and Figure S15 for values). These values are overlaid onto the parametric analysis in Figure 5c and d, which gives excellent agreement with observed temperature coefficients. The temperature has the greatest effect in $BiVO_4$ because the majority of the light is absorbed within the temperature-enhanced quasi-neutral region.

In summary, we developed and validated an analytical model describing the dependence of the photocurrent on both temperature and radius of nanowires. The temperature-dependent minority carrier diffusion length was quantitatively extracted by fitting this model to the thermally enhanced photocurrent on the radius-controlled nonstoichiometric, rutile TiO_{2-x} nanowires, confirming unambiguously that the minority carrier diffusion length increases with temperature. Our observation reveals that the relative magnitudes of minority carrier diffusion length to depletion layer width establish the extent of temperature enhancement in the oxides exhibiting Arrhenius-type minority carrier diffusion length, and quantitatively explains the different photocurrent temperature coefficients in $BiVO_4$, TiO_2, and α-Fe_2O_3.

Methods. *Materials.* Titanium(IV) isopropoxide (TTIP, 97%), sodium chloride (NaCl, ≥99%), sodium hydroxide (NaOH, ≥97%), sodium sulfite (Na_2SO_3, ≥98%), potassium hexacyanoferrate (III) ($K_3Fe(CN)_6$, ≥99.0%), and potassium hexacyanoferrate(II) trihydrate ($K_4Fe(CN)_6{\cdot}3H_2O$, ≥ 99.95%) were purchased from Sigma-Aldrich. Hydrochloric acid (HCl, ≥36.5%) was purchased from Fisher Chemical. All chemicals were used as purchased. Solutions were prepared using high-purity water (Millipore Milli-Q purification system, resistivity ≥18.2 MΩ·cm). Glass wafers coated with fluorine-doped tin oxide (FTO) were purchased from MTI.

Synthesis of TiO_2 Nanowire Array. TiO_2 nanowire arrays were prepared on FTO via a hydrothermal method. For a typical synthesis, DI water (8 mL) was mixed with HCl (8 mL 36.5–38.0%) and stirred for 5 min before TTIP (0.18 mL) was slowly added. To reduce the radius of TiO_2 nanowires, 2.0 mL of NaCl saturated solution (the ratio between precursor/NaCl equals to 1/20) was added into the aqueous solution. After stirring for at least 1 h, the mixture was transferred to a Teflon-lined stainless steel autoclave. Clean FTO/glass substrates were immersed with the conducting side face down. The autoclave was put in an oven at a temperature of 180 °C and was taken out from the oven after 150 min. To increase the radius of TiO_2 nanowires, 0.27 mL of TTIP was added into the same mixture of HCl/DI water, and the reaction was controlled at 180 °C for 100 min. After the autoclave was cooled to room temperature, the FTO substrate was rinsed with DI water, blown with high-purity nitrogen, and subsequently annealed at 400 °C for 2 h in air.

Creating Oxygen Vacancies. The obtained TiO_2 nanowire array was subsequently treated in a hydrogen environment balanced with water vapor at 325–425 °C for 30 min to create oxygen vacancies. The water vapor was introduced by a flow-through humidity generator (P-10, Cellkraft, Stockholm, Sweden), which controls the volume percent of water by heating a water bath at 40 °C and allowing water vapor to pass through a water-selective Nafion membrane. Pure argon (50 sccm) carrier gas was flowed across the membrane with 0.5 vol % of water vapor and diluted by pure hydrogen (200 sccm, reaction gas) before entering the oven. After hydrogen treatment, the sample is cooled down naturally in the same atmosphere and then washed with DI water.

Physical Characterization. The morphology of the TiO_{2-x} nanowire array was examined by scanning electron microscopy (SEM, FEI-XL 30 Sirion). To assess the phase purity and crystallinity, TEM and XRD were carried out using a FEI-Titan

DOI: 10.1021/acs.nanolett.7b01504
Nano Lett. 2017, 17, 5264–5272

(taken at 100 keV) and powder X-ray diffraction D8 system (Cu K_α radiation).

Photoelectrochemical Measurements. The PEC characterization was carried out in a homemade temperature-controlled cell, which was immersed in a water bath connected to a thermostatic circulator. The cell temperature was measured via a Teflon-coated thermocouple located adjacent to the electrode. The typical variation for a given temperature set point was ±0.5 °C. Photocurrent measurements were carried out using a solar simulator (350 to 1100 nm, HAL-320, Asahi Spectra Inc.), the spectrum of which has been verified by a UV−vis spectrometer (USB 2000+, Ocean Optics). The illumination intensity was calibrated to achieve 1 sun condition (79 mW/cm^2) in the wavelength range of 350−1100 nm.

A Pt wire and a reversible hydrogen electrode (RHE, eDAQ Inc.) were used as the CE and RE, respectively. The WE was sealed by an O-ring in the homemade cell, and the electrolyte was purged by argon for 20 min before and during each measurement. All photocurrent measurements in this work were conducted in a 1 M NaOH solution. In some experiments, 0.1 M Na_2SO_3 was added to the electrolyte as a hole scavenger to speed up the kinetics of the reaction at the electrode/electrolyte interface. For the IPCE measurement, the solar simulator was coupled with a monochromator (CMS-100, Asahi Spectra Inc.) to sweep the wavelength of the incident light. To reveal the accurate IPCE under a 1 sun condition, a second solar-simulated light was coupled into the monochromatic light as a white light bias via a 50:50 beam splitter. The overall incident light spectrum and intensity were verified by a UV−vis spectrometer. The IPCE was then calculated from the photocurrent measured at 1.0 V vs RHE, according to the following equation:

$$\mathrm{IPCE} = \frac{J_{\mathrm{ph}}(\mathrm{mA\,cm^{-2}}) \times 1239.8(\mathrm{V\,nm})}{P_{\mathrm{mono}}(\mathrm{mW\,cm^{-2}}) \times \lambda(\mathrm{nm})}$$

The open-circuit potential (OCP) was measured in a 1 M NaOH solution containing a 1 mM $[Fe(CN)_6]^{3-}$/10 mM $[Fe(CN)_6]^{4-}$ reversible redox couple. At a concentration ratio of 1:10, the couple has an equilibrium potential of +0.302 V vs NHE,[34] which is close to the equilibrium potential for OER in a strong basic electrolyte. Thus, one can expect the built-in voltage at the TiO_{2-x}/electrolyte interface in the presence of the ferricyanide couple is similar to that without the redox couple. Back illumination was applied in the OCP measurement to eliminate light absorption from the brown colored electrolyte containing the reversible redox couple.

The Mott−Schottky measurements were performed using the staircase potentio electrochemical impedance spectroscopy (SPEIS), which performed a successive impedance measurement (on a whole frequency range) during a DC potential scan. Mott−Schottky curves are plotted C_{sc}^{-2} (C_{sc} is presumably the space-charge capacitance) as a function of applied potential.

Simulation. The photocurrent temperature coefficient was simulated based on a one-dimensional model using Matlab. The detailed assumption and simulation procedures are described in the Supporting Information. All 15 data points were fitted together to obtain the optimal W, L_0, and E_a values.

■ ASSOCIATED CONTENT

Supporting Information

The Supporting Information is available free of charge on the ACS Publications website at DOI: 10.1021/acs.nanolett.7b01504.

Detailed information for nanowire characterization; oxygen vacancy estimation; stability evaluation; simulation and fittings; comparison of space charge layer thickness and minority carrier diffusion length in three photoanodes (PDF)

■ AUTHOR INFORMATION

Corresponding Author

*Address: Department of Materials Science and Engineering, Stanford University, 496 Lomita Mall, Stanford, CA 94305. Tel.: (+)1-650-725-7515. E-mail: wchueh@stanford.edu.

ORCID

William C. Chueh: 0000-0002-7066-3470

Author Contributions

L.Z. and L.S. contributed equally to this work. L.Z. and W.C.C. conceived the experiment. L.Z. and L.S. synthesized the photoelectrodes and carried out the photoelectrochemical measurements. S.L. performed the TEM characterization. L.Z., Z.G., Y.L., H.D., and Y.L. carried out the modeling and data fitting. N.L.A. calculated the oxygen vacancy concentration. All coauthors discussed the results and participated in writing the manuscript.

Notes

The authors declare no competing financial interest.

■ ACKNOWLEDGMENTS

This work was funded by the Precourt Institute for Energy and the Global Climate and Energy Project at Stanford University and was also supported by the National Science Foundation under award No. 1336835.

■ REFERENCES

(1) Walter, M. G.; Warren, E. L.; McKone, J. R.; Boettcher, S. W.; Mi, Q.; Santori, E. A.; Lewis, N. S. *Chem. Rev.* **2010**, *110*, 6446−6473.

(2) Alexander, B. D.; Kulesza, P. J.; Rutkowska, I.; Solarska, R.; Augustynski, J. *J. Mater. Chem.* **2008**, *18*, 2298−2303.

(3) Morin, F. J. *Phys. Rev.* **1954**, *93*, 1195−1199.

(4) Goodenough, J.; Zhou, J. S. *Chem. Mater.* **1998**, *10*, 2980−2993.

(5) Rettie, A. J.; Lee, H. C.; Marshall, L. G.; Lin, J. F.; Capan, C.; Lindemuth, J.; McCloy, J. S.; Zhou, J.; Bard, A. J.; Mullins, C. B. *J. Am. Chem. Soc.* **2013**, *135*, 11389−11396.

(6) Afifi, M. A.; Abdel-Aziz, M. M.; Yahia, I. S.; Fadel, M.; Wahab, L. A. *J. Alloys Compd.* **2008**, *455*, 92−97.

(7) Simon, M. Z.; Kwok, K. Ng. *Physics of Semiconductor Devices*; John Wiley & Sons: New York, 2007.

(8) Zhang, L. M.; Ye, X. F.; Boloor, M.; Poletayev, A.; Melosh, N. A.; Chueh, W. C. *Energy Environ. Sci.* **2016**, *9*, 2044−2052.

(9) Ye, X.; Yang, J.; Boloor, M.; Melosh, N. A.; Chueh, W. C. *J. Mater. Chem. A* **2015**, *3*, 10801−10810.

(10) Brunauer, G. C.; Rotter, B.; Walch, G.; Esmaeili, E.; Opitz, A. K.; Ponweiser, K.; Summhammer, J.; Fleig, J. *Adv. Funct. Mater.* **2016**, *26*, 120−128.

(11) Walch, G.; Rotter, B.; Brunauer, G. C.; Esmaeili, E.; Opitz, A. K.; Kubicek, M.; Summhammer, J.; Ponweiser, K.; Fleig, J. *J. Mater. Chem. A* **2017**, *5*, 1637−1649.

(12) Haussener, S.; Hu, S.; Xiang, C.; Weber, A. Z.; Lewis, N. S. *Energy Environ. Sci.* **2013**, *6*, 3605−3618.

(13) Leamy, H. J. *J. Appl. Phys.* **1982**, *53*, R51−R80.

DOI: 10.1021/acs.nanolett.7b01504
Nano Lett. 2017, 17, 5264−5272

(14) Wu, C. J.; Wittry, D. B. *J. Appl. Phys.* **1978**, *49*, 2827−2836.
(15) Boudjani, A.; Bassou, G.; Benbakhti, T.; Beghdad, M.; Belmekki, B. *Solid-State Electron.* **1995**, *38*, 471−475.
(16) Orton, J. W.; Blood, P. *The Electrical Characterization of Semiconductors: Measurement of Minority Carrier Properties*; Academic Press, London, 1990.
(17) Navas, J.; Guillen, E.; Alcantara, R.; Fernandez-Lorenzo, C.; Martin-Calleja, J.; Oskam, G.; Idigoras, J.; Berger, T.; Anta, J. A. *J. Phys. Chem. Lett.* **2011**, *2*, 1045−1050.
(18) Lana-Villarreal, T.; Monllor-Satoca, D.; Gómez, R.; Salvador, P. *Electrochem. Commun.* **2006**, *8*, 1784−1790.
(19) Pala, R. A.; Leenheer, A. J.; Lichterman, M.; Atwater, H. A.; Lewis, N. S. *Energy Environ. Sci.* **2014**, *7*, 3424−3430.
(20) Cronemeyer, D. C. *Phys. Rev.* **1952**, *87*, 876−886.
(21) Colbeau-Justin, C.; Kunst, M.; Huguenin, D. *J. Mater. Sci.* **2003**, *38*, 2429−2437.
(22) Salvador, P. *J. Appl. Phys.* **1984**, *55*, 2977−2985.
(23) Seabold, J. A.; Choi, K. S. *J. Am. Chem. Soc.* **2012**, *134*, 2186−2192.
(24) McDonald, K. J.; Choi, K. S. *Energy Environ. Sci.* **2012**, *5*, 8553−8557.
(25) Rao, P. M.; Cai, L. L.; Liu, C.; Cho, I. S.; Lee, C. H.; Weisse, J. M.; Yang, P. D.; Zheng, X. L. *Nano Lett.* **2014**, *14*, 1099−1105.
(26) Kayes, B. M.; Atwater, H. A.; Lewis, N. S. *J. Appl. Phys.* **2005**, *97*, 114302.
(27) Liu, B.; Aydil, E. S. *J. Am. Chem. Soc.* **2009**, *131*, 3985−3990.
(28) Hwang, Y. J.; Hahn, C.; Liu, B.; Yang, P. D. *ACS Nano* **2012**, *6*, 5060−5069.
(29) Wang, G. M.; Wang, H. Y.; Ling, Y. C.; Tang, Y. C.; Yang, X. Y.; Fitzmorris, R. C.; Wang, C. C.; Zhang, J. Z.; Li, Y. *Nano Lett.* **2011**, *11*, 3026−3033.
(30) Shin, J. Y.; Joo, J. H.; Samuelis, D.; Maier, J. *Chem. Mater.* **2012**, *24*, 543−551.
(31) Marucco, J.; Gautron, J.; Lemasson, P. *J. Phys. Chem. Solids* **1981**, *42*, 363−367.
(32) Alcock, C. B.; Zador, S.; Steele, B. C. H. *Electromotive Force Measurements in High Temperature Systems*; Alcock, C. B., Ed.; Institute of Mining and Metallurgy: London, 1968.
(33) Cho, I. S.; Logar, M.; Lee, C. H.; Cai, L. L.; Prinz, F. B.; Zheng, X. L. *Nano Lett.* **2014**, *14*, 24−31.
(34) Dean, J. A. *Lange's Handbook of Chemistry*, 13th ed.; McGraw Hill Book Company: New York, 1985.
(35) Bard, A. J.; Faulkner, L. R. *Electrochemical Methods: Fundamentals and Applications*; John Wiley & Sons, Inc., 2001.
(36) Liu, M.; Yu, B.; Xu, J.; Chen, J. *J. Power Sources* **2008**, *177*, 493−499.
(37) Vernon, S.; Anderson, W. *Appl. Phys. Lett.* **1975**, *26*, 707−709.
(38) Hovel, H.; Woodall, J. *J. Electrochem. Soc.* **1973**, *120*, 1246−1252.
(39) Anderson, A. B.; Roques, J. M.; Mukerjee, S.; Murthi, V. S.; Markovic, N. M.; Stamenkovic, V. *J. Phys. Chem. B* **2005**, *109*, 1198−1203.
(40) Sheng, W.; Gasteiger, H. A.; Yang, S. H. *J. Electrochem. Soc.* **2010**, *157*, B1529−1536.
(41) Dotan, H.; Kfir, O.; Sharlin, E.; Blank, O.; Gross, M.; Dumchin, I.; Ankonina, G.; Rothschild, A. *Nat. Mater.* **2012**, *12*, 158−164.
(42) Abdi, F. F.; Savenije, T. J.; May, M. M.; Dam, B.; van de Krol, R. *J. Phys. Chem. Lett.* **2013**, *4*, 2752−2757.
(43) Zhao, X.; Luo, W. J.; Feng, J. Y.; Li, M. X.; Li, Z. S.; Yu, T.; Zou, Z. G. *Adv. Energy Mater.* **2014**, *4*, 1301785.
(44) Zhong, D. K.; Cornuz, M.; Sivula, K.; Grätzel, M.; Gamelin, D. R. *Energy Environ. Sci.* **2011**, *4*, 1759−1764.
(45) Kennedy, J. H.; Frese, K. W. *J. Electrochem. Soc.* **1978**, *125*, 709−714.

DOI: 10.1021/acs.nanolett.7b01504
Nano Lett. 2017, 17, 5264−5272